Marine and Petroleum Geology 177 (2025) 107406

Contents lists available at ScienceDirect

Marine and Petroleum Geology

journal homepage: www.elsevier.com/locate/marpetgeo

Effects of outcrop-scale structural and diagenetic heterogeneities on flow and mass transport in a porous sandstone aquifer

Marco Antonellini [a,*], Leonardo Del Sole [a,*], Pauline Nella Mollema [b]

[a] Department of Biological, Geological, and Environmental Sciences, University of Bologna, Bologna, Italy
[b] Terraporosa Consulting, Italy

A B S T R A C T

We apply outcrop-based structural and *in-situ* petrophysical properties measurements for the construction of flow and mass transport calibrated numerical models in a porous sandstone aquifer. The hydraulic conductivity in this aquifer is influenced by the presence of deformation bands and related carbonate nodules. These heterogeneities are shown to decrease the hydraulic conductivity of the host rock by 2–3 orders of magnitude. The result obtained is robust, given that the models were calibrated with hydrologic field data. Our upscaling methodology for hydraulic conductivity allows inclusion of outcrop-scale structures and diagenetic features by means of inversion of the advective velocity for conservative particles. This approach can be used for easily implementing field data in aquifers or other geofluids reservoir simulators. Our experiments show that the use of an equivalent isotropic hydraulic conductivity approach fails to correctly account for mass transport in porous sandstone aquifers and we recommend implementing, as much as possible, the local heterogeneities and anisotropies in hydraulic conductivity within the model to be able to have a more realistic and conservative estimate of advection and dispersion. Our findings should be helpful to those scientists dealing with geofluids modeling and groundwater pollution.

1. Introduction

Deformation bands and related diagenetic features such as pore-filling cement affect the textural properties of porous reservoir rocks as well as their petrophysical and mechanical properties (Aydin and Johnson, 1978; Antonellini et al., 1994; Antonellini and Aydin, 1994). Such heterogeneities influence fluid flow in terms of anisotropy, compartmentalization, and flow rate. Also, it is still a matter of debate where these structures could be pathways and where they could be barriers for fluids (Antonellini and Aydin, 1994; Aydin, 2000; Shipton et al., 2005; Fossen et al., 2007; Torabi and Fossen, 2009; Ballas et al., 2015; Zuluaga et al., 2016; Rotevatn et al., 2017; Awdal et al., 2020; Romano et al., 2021; Del Sole et al., 2020b; Souza et al., 2022).

Deformation bands are small "fault-like" mm-thick tabular structures that commonly develop in granular or porous sediments and sedimentary rock (e.g., Antonellini and Aydin, 1994). They may result from non-destructive granular flow (i.e., translation, grain rotation; Rawling and Goodwin, 2003), or cataclasis, (Aydin et al., 2006; Fossen et al., 2007; Nogueira et al., 2021). The impact that these structures have on fluid flow within porous reservoirs depends on specific factors including the permeability contrast with respect to the host rock, their frequency, thickness, spatial and geometrical distribution, segmentation, and connectivity (Antonellini and Aydin, 1994, 1995; Gibson, 1998; Manzocchi et al., 1998; Sternlof et al., 2004; Shipton et al., 2005; Fossen and Bale, 2007; Del Sole et al., 2020a; Pourmalek et al., 2021; Aydin et al., 2023). In high porosity rocks, cataclasis accompanied by grain crushing and rearrangement due to shearing generates deformation bands with compacted fabric called compactive shear bands (CSBs from now on), which imply an important reduction in porosity and permeability. For this reason, CSBs associated with cataclasis inhibit or buffer the fluid flow (Antonellini and Aydin, 1994; Antonellini et al., 1994, 1999; Mollema and Antonellini, 1996; Aydin, 2000; Bense et al., 2003; Fossen et al., 2007; Del Sole and Antonellini, 2019). On the other hand, deformation bands with a component of dilation may enhance and channel fluid flow (Du Bernard et al., 2002; Bense et al., 2003).

In general, permeability in an aquifer is influenced by all sorts of structures besides deformation bands, for example joints, veins, reactivated or sheared older structures and more. Therefore, the upscaled permeability refers to an "equivalent" or "effective" permeability, which accounts for the combined effect of matrix and all types of fractures present at specific spatial scale (e.g., Bisdom et al., 2016a; Bisdom et al., 2016b; Dewandel et al., 2012; Medici et al., 2023). Typically, joints increase the equivalent permeability by two orders of magnitude (Taylor et al., 1999). CSBs, instead, reduce permeability by 1–6 orders of magnitude (Antonellini and Aydin, 1994; Matthäi et al., 1998; Taylor and Pollard, 2000; Jourde et al., 2002; Del Sole et al., 2020a; Aydin

* Corresponding authors.
E-mail addresses: m.antonellini@unibo.it (M. Antonellini), leonardo.delsole@unibo.it (L. Del Sole).

https://doi.org/10.1016/j.marpetgeo.2025.107406
Received 7 February 2025; Received in revised form 26 March 2025; Accepted 3 April 2025
Available online 4 April 2025

et al., 2023). This implies that small-scale geological features like CSBs, which accommodate only small sub-seismic resolution offsets from a few mm up to 1.5 m, affect subsurface fluid flow, promoting reservoir compartmentalization, anisotropy and causing buffering or sealing during production (Harper and Moftah, 1985; Edwards et al., 1993; Antonellini and Aydin, 1994; Fowles and Burley, 1994; Gibson, 1998; Manzocchi et al., 1998; Antonellini et al., 1999, 2014; Rawling et al., 2001; Sternlof et al., 2006; Fachri et al., 2013a, 2013b; Zuluaga et al., 2016; Pourmalek et al., 2021; Romano et al., 2021). In addition to deformation structures, sandstone reservoirs are often associated with pore-filling cement in the form of nodules of different shapes and arrangements (McBride et al., 1995; Mozley and Davis, 2005; Del Sole et al., 2020a). Porosity within nodules (or concretions) may be entirely filled with cement strongly affecting fluid circulation.

The outcrops we worked on show several sets of CSBs, aligned with cement precipitation zones in the pore space. Similar outcrops were also described previously in the area (Antonellini and Mollema, 2002; Del Sole and Antonellini, 2019; Del Sole et al., 2020a). In this paper, however, we want to establish the influence of the presence of CSBs and nodules on the equivalent permeability and general hydraulic behavior of a heterogeneous sandstone aquifer.

Our flow simulations help to quantify the contrast in permeability between CSBs associated with nodules and host rock. Moreover, transport simulations permit to upscale the field permeability from the scale of structures in the outcrop (cm) to the scale of model cells (10 m). The investigation of the petrophysical properties of these structures is crucial in the evaluation of their impact on the subsurface fluid flow. Petrophysical data collected at the scale of deformation bands are important in the characterization of the aquifer and they are a good starting point in the construction of regional numerical flow models. In a flow model, the hydraulic properties of the rock are defined at each cell (or node) of the grid, typically represented by a permeability (or hydraulic conductivity) tensor K and effective porosity (e.g., Antonellini et al., 2014). In the case of field permeability measurements, they give information only at the mm to cm scale of a single CSB or zones of a few to tens of CSBs. It is difficult to construct a regional model (scale of kilometers) with a cell size characterized by this fine resolution, for computational reasons. It is therefore important to up-scale the permeability measured in the field to the cell size of the model (Antonellini et al., 2014).

Several numerical flow models considering the effects of deformation bands have been published starting from the early work of Matthäi et al. (1998) both considering an Equivalent Porous Medium (EPM) approach (Zuluaga et al., 2016; Awdal et al., 2020; Berge et al., 2022; Souza et al., 2022) and/or a Discrete Fracture Network (DFN) approach (Antonellini et al., 2014) but, to the best of our knowledge, there have not been systematic attempts to calibrate the models with field data. More recently, Berge et al. (2022) explicitly used fine-scale numerical simulations that include deformation bands for a wide range of stochastically generated networks to upscale the permeability at that of the reservoir cell block at the CO_2 storage site of Smeaheia in the North Sea. By using this methodology, they show that deformation bands with a permeability contrast higher than three orders of magnitude with respect to the host rock may strongly reduce fluid flow through faults.

The scale at which the published models have been applied ranges from the size of a small hand sample or core plug (cm-scale; Zambrano et al., 2018; Zambrano et al., 2021) to that of field reservoirs (km-scale; Berge et al., 2022). The models that we present in this paper go from the scale of a single flow simulator cell (outcrop model of 10 m in our case) to that of a field scale aquifer (km-scale) and, therefore, span the scales of most models presented in the literature. Furthermore, the upscaling procedure by particle tracking and advective transport appears to be a fast and reliable process to directly import field permeability data at micro/meso-scales into models at increasingly larger observation scales.

Our numerical simulations provided insight into the effects that CSBs and carbonate nodules have on dispersion, which is important for evaluating the movement of pollutants within an aquifer or the sweeping capacity of injected fluids during enhanced geofluids recovery. This is a novel theme that we deal with in our work.

In summary the specific objectives of our work are the following: (i) Establish quantitatively the effect that deformation bands and associated diagenetic structures have on the aquifer (or reservoir) scale by using calibrated numerical models. (ii) Develop an upscaling methodology that allows effectively and easily import *in-situ* petrophysical measurements at mesoscale into an aquifer (or reservoir) model. (iii) Explore the effects that CSBs and diagenetic nodules have on macroscale dispersion driven by the interaction of advective velocity with heterogeneities in hydraulic conductivity.

2. Study area

The study area (Fig. 1) includes well-exposed outcrops of Loiano sandstone in the Northern Apennines (Emilian Apennines), 20 km south of the city of Bologna. The Loiano Sandstones are considered a mountain aquifer with poor hydraulic characteristics (Sorgenti e unità geologiche sede di acquiferi nell'Appennino emiliano-romagnolo - Geologia, suoli e sismica - Ambiente, 2009). The Northern Apennines are a fold-and-thrust belt composed of NE verging tectonic units and developed during the Cenozoic collision between the European plate (Corso-Sardinian Block) and the Adria plate (Boccaletti and Guazzone, 1974; Marroni and Treves, 1998; Boccaletti et al., 2011).

This work focuses on the Loiano Sandstones that are exposed between the Savena Valley in the west and the locality of Loiano in the east (Cibin et al., 2001; Antonellini and Mollema, 2002). The Loiano Sandstones are part of the Monte Piano Fm which, in turn, is part of the Epiligurian Monte Piano-Loiano-Ranzano (MLR) Sequence, deposited from the Middle Eocene to the Upper Oligocene (Fig. 1; Valloni and Zuffa, 1984; Cibin et al., 2001; Antonellini and Mollema, 2002; Conti et al., 2016). The Epiligurian Succession is a complex sedimentary sequence deposited into piggy-back basins resting, discordant, on top of Ligurian thrust sheets, (Ori and Friend, 1984; Bettelli and Vannucchi, 2003; Remitti et al., 2012; Piazza et al., 2016; Conti et al., 2020; Stendardi et al., 2023). These basins migrated passively to the NE during the Apennines Orogeny (Ricci Lucchi, 1986; Vai and Martini, 2001). The complete stratigraphic succession spans in age from the Middle Eocene to the Late Miocene or the earliest Pliocene (Conti et al., 2020). The sedimentation in the Epiligurian basins was continuous and they were only mildly affected by multiple tectonics events during the NE migration of the accretionary wedge (Cibin et al., 2001; Antonellini and Mollema, 2002).

The Loiano Sandstones are a 300–1000 m thick lenticular body, late Lutetian-Bartonian in age, representing proximal turbiditic deposits of poorly consolidated, immature, and high porosity arkosic sandstones and conglomerates (49–60 % quartz, 39–48 % feldspar; Ricci Lucchi, 1986; Cibin et al., 1993; Del Sole and Antonellini, 2019). The maximum burial depth of the Loiano Sandstones is estimated to be 3 km, which is typical for low-depth diagenetic processes such as compaction and intergranular cementation (Cibin et al., 1993; Antonellini and Mollema, 2002). The structures in the upper and lower stratigraphic sections of these sandstones are characterized by multiple sets of CSBs associated with carbonate nodules generated by local precipitation of calcite cement in the interstitial pore space of the host rock (Del Sole and Antonellini, 2019). Most nodules (75 %) are parallel to CSBs, whereas the remaining are bedding-parallel (25 %). The elongation of nodules, along and parallel to CSBs or their presence at the intersection between two different sets of CSBs, demonstrates the geometrical association between nodules and deformation structures.

3. Methods

3.1. Outcrop characterization

The study area extends along a 2-km-wide E-W–oriented belt around

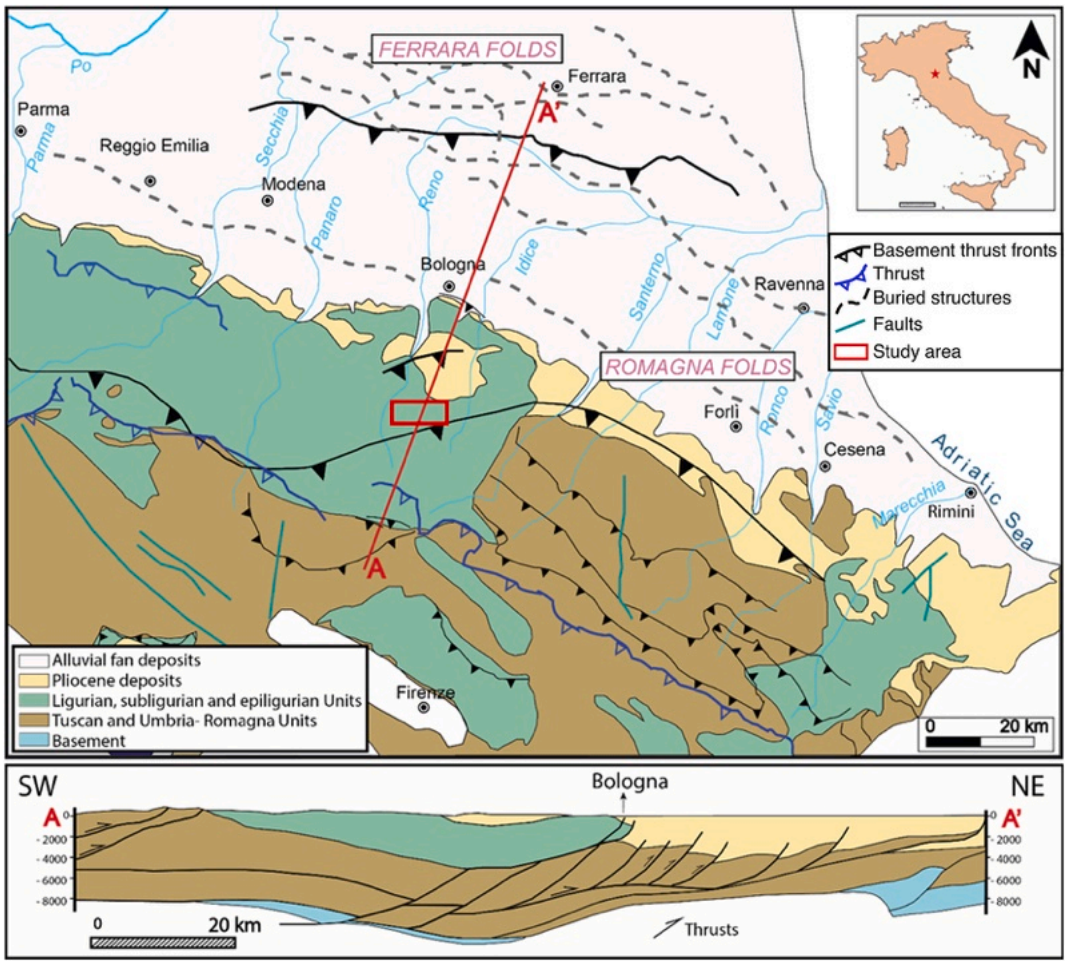

Fig. 1. Location of the study area (red rectangle) where the Loiano Sandstones are outcropping in the Northern Apennines. The Loiano sandstones belong to the Monte Piano-Loiano-Ranzano Sequence, which is the lowermost (stratigraphically) Epiligurian unit (light green). The cross section below shows the fold and thrust belt structural setting of the study area. (For interpretation of the references to colour in this figure legend, the reader is referred to the Web version of this article.)

the village of Loiano (Fig. 2). The offsets of CSBs and their frequency within the Loiano Sandstones were evaluated by measuring structural and frequency data along nine several meters long transects distributed over the study area, some of which were combined to have data in two perpendicular directions (Fig. 2). The position of the transects was recorded through a GPS mobile device. At each transect, the orientation of CSBs was measured using a Brunton geological compass, and data were reported in a topographic map (scale 1: 2,000) using the Clino™ App. Stereographic projections and azimuthal analysis of structural data were then made using the Daisy3 software (Salvini, 2002). CSBs were characterized into those oriented along calcite nodules and those that were not. CSBs and nodule patterns, as well as their characteristics and spatial relationships, were also documented in field digital photographs, drone imagery (Fig. 3), and high-resolution orthophoto mosaics.

A detailed geologic field map of DBs was constructed (original scale 1:5000). The traces of CSBs planes were extrapolated with geometric projection techniques. The map was then digitized in QGIS (QGIS Development Team, 2021), and a shapefile was created for further inclusion into MODFLOW (Harbaugh, 2005).

The free water surface of tributary streams to the nearby Savena River was measured using a GPS mobile device. These points represent control points for calibration in the modeling phase.

3.2. Numerical modeling

We say up front that in this study we will use hydraulic conductivity instead of permeability, because we work with aquifer numerical models.

The numerical modeling methodology consists of two independent workflows, which are schematically explained in Fig. 4.

In the first workflow (upper part of Fig. 4), regional flow models (**R**) for the Loiano Sandstones at the km-scale were constructed in MODFLOW-2005, a three-dimensional finite difference water flow simulator developed by the U.S. Geological Survey (Harbaugh, 2005; Harbaugh et al., 2017). The models are then calibrated with field data (reported in Table 1 and published in Del Sole et al., 2020a) in a way to obtain the equivalent hydraulic conductivity (or upscaled K) of a single cell (10 m × 10 m x 500 m). The vertical length of the cell (500 m) comes from the choice of using an average vertical conductivity due to the homogeneity of the section and by being the structures sub-vertical; this reduces also computation times. These models provide information on the hydraulic head distribution and once imported into MODPATH (Pollock, 2016, 2017), allow to evaluate the flow field and mass transport within the aquifer (advection and dispersion).

In the second workflow (lower part of Fig. 4), the numerical modeling is performed on a domain, which corresponds to the single cell of the first, regional, model (**R**). This is done to upscale the in-situ measured-petrophysical properties. The single cells of these models (**LMU** – local models for upscaling) are 0.1 m × 0.1 m x 10 m. The measured *in-situ* petrophysical properties (Del Sole et al., 2020a, Table 1) of the host sandstone, the carbonate nodules, and the CSBs are set to the individual cell scale. In this way, the individual cells have the

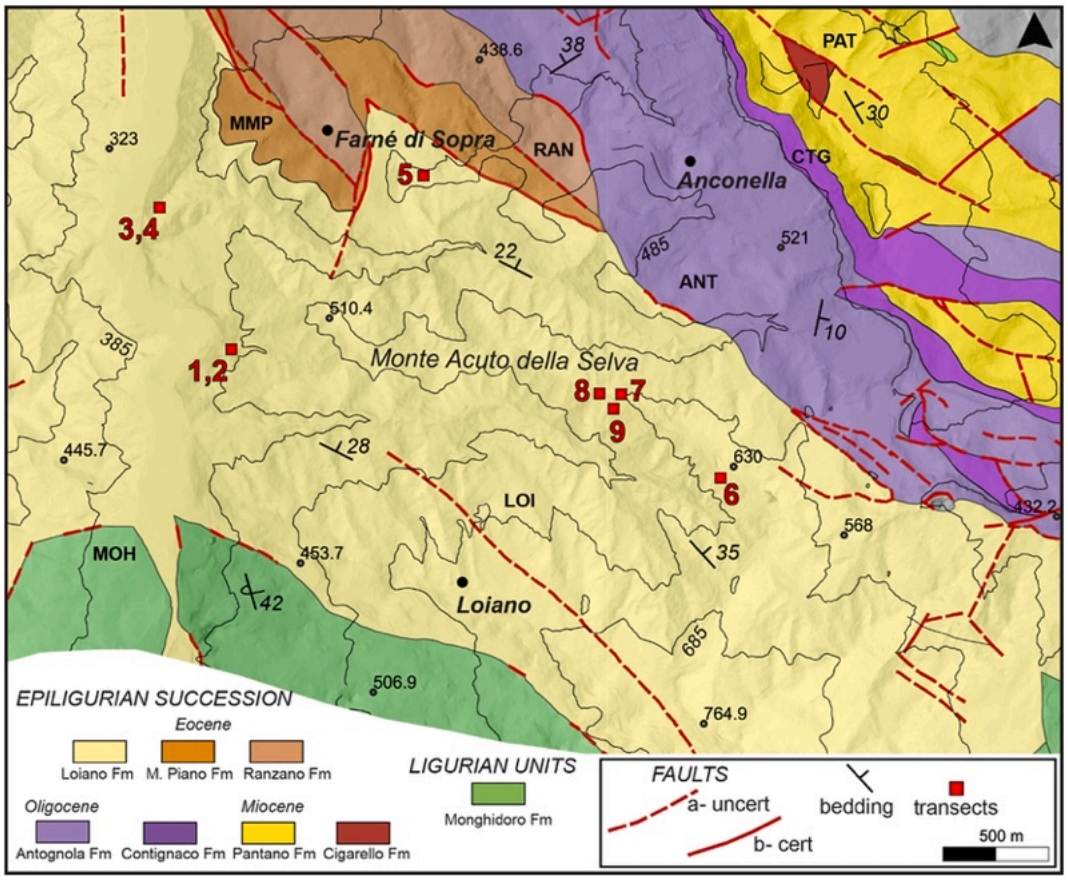

Fig. 2. Position of the transects measured in the study area. Where two numbers are present, two transects perpendicular to each other have been measured.

properties of nodules and zone of bands measured *in-situ*. These local flow models are then used to derive particle advective velocities using MODPATH and in turn, these are used to calculate the average hydraulic conductivity of the model domain. This is the upscaled hydraulic conductivity obtained from the outcrop data. We compare this with the equivalent hydraulic conductivity for the whole regional model (**R**).

3.2.1. *Regional models settings*

The regional models (**R**; Fig. 5a and b) were set up in ModelMuse (Winston, 2019, 2020), that is a graphical user interface (GUI) developed by U.S. Geological Survey for MODFLOW-2005 (Harbaugh, 2005). The models domain was generated based on a shapefile polygon imported from QGIS (QGIS Development Team, 2021) and extrapolated from the geological map. It outlines a section of the Loiano Sandstones from the watershed-divide to the bottom of the valley with a surface area of 6 km^2 and a thickness of 500 m, which is the total thickness of the Loiano Sandstones. The models have 61.000 cells of 10 × 10 × 500 m each. The choice of cell dimensions was decided to avoid long computational times and to maintain a good spatial resolution even within a large area. A 5-m resolution Digital Elevation Model (DEM) was imported and interpolated at the models surface.

The northern and southern boundaries of the regional models are lithological contacts, modeled as no-flow boundaries. The Loiano Sandstones are in lithological contact with the Monghidoro Fm at their base, and the Monte Piano and Antognola Fms at the top. Both units are rich in clay and act as aquicludes or aquitards. The eastern side of the model is a no-flow boundary as it represents a topographic watershed-divide. The western boundary of the model is a drain boundary condition with a conductance of 100 m^3/d. This corresponds to the river with its free surface at 320 m.

The amount of recharge applied at the topographic top of the models is based on precipitation data downloaded from the webapp Dext3r of ARPAE ("Agenzia per la Protezione Ambientale"; https://simc.arpae.it/dext3r/) – Emilia Romagna for the years 2022 and 2023 (periods of water level measurements in the creeks). Considering evapotranspiration and runoff, recharge was assumed to be 50 % of the total amount of precipitation in one year (0.001 m/d; ARPAE ; https://webbook.arpae.it/).

In regional models **R** case **1**, **2**, **3**, and **4**, the shapefile of CSBs was imported into ModelMuse as a polyline object, and the hydraulic conductivity and porosity of the host rock and upscaled CSBs (procedure explained in *3.2.3*) were assigned. In this way, all cells intersecting CSBs get the same upscaled hydraulic conductivity value.

3.2.2. *Numerical experiments and calibration process*

The numerical regional model (**RH**) simulating single-phase steady state flow was used to obtain homogeneous hydraulic conductivity for the aquifer, combining the effects of the matrix, of the CSBs, and the carbonate nodules. For this purpose, calibration was carried out by matching the heads measured in the field with the heads calculated by the simulations. The hydraulic conductivity was changed until a best fit was obtained (Cheong et al., 2008; Khadri and Moharir, 2016). After each simulation, the difference between calculated and observed hydraulic heads as well as the percent discrepancy values in the water budget, were recorded. During the simulations, the convergence criterion was equal to 1 % (Ahlfeld and Hoque, 2008).

The next step of the regional modeling process (**R** cases **1**, **2**, **3**, and **4**) included CSB zones and carbonate nodules as hydraulic conductivity heterogeneities. The "Parameter ESTimation" (PEST) package with MODFLOW (Doherty, 2015) was used for input generation of K. The hydraulic conductivity was assumed to be isotropic within the matrix and within the CSBs and their initial values were those in Table 1. PEST's

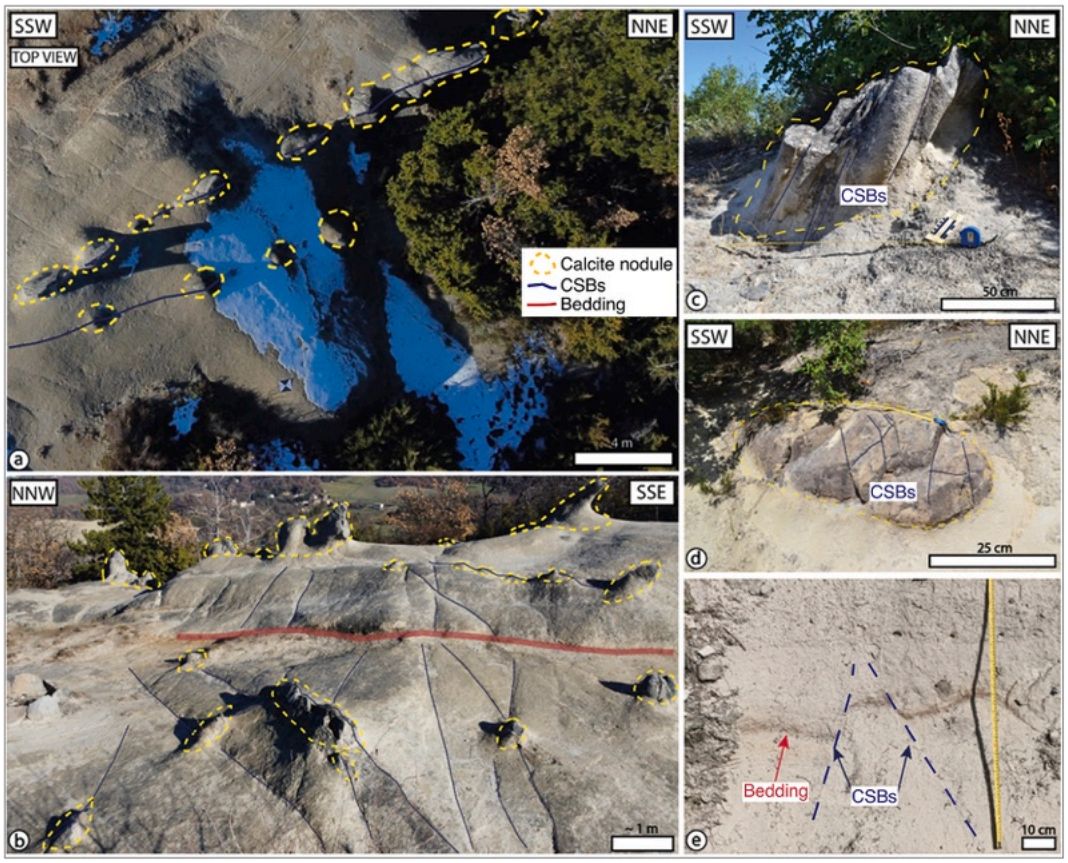

Fig. 3. Photographs of the outcrops in the Loiano Sandstones. (a) Orthorectified photograph from drone imagery showing the alignment of nodules along CSBs. (b) Panoramic field photographs of the outcrop in (a). The red line indicates bedding. Yellow dashed lines identify carbonate nodules. (c) Carbonate nodule along a zone of CSBs (thin blue lines). (d) Isolated nodule associated with three different sets of CSBs. (e) Detail of the reddish silt layer shown in (b) where it is offset by a thin CSBs up to 15 cm. The apparent sense of offset is normal. (For interpretation of the references to colour in this figure legend, the reader is referred to the Web version of this article.)

role is to minimize the weighted sum of squared differences between calculated values of some property, and those observed in the laboratory or field; this weighted sum is referred to as the "objective function" (Doherty, 2015). The purpose of the simulations was to investigate K combinations of host rock and CSBs, for which the "objective function" was minimized. The calibration and simulation results are presented in Table 3. The Regional Isotropic model obtained by manual calibration is in the first line (**RH**). The following four lines report the regional models obtained with PEST calibration; **R1** allowing for K_{hr} and K_{CSB} to vary – **R2**, **R3**, and **R4** allowing only K_{CSB} to vary and fixing K_{hr} at different values. The last three lines report the results for the local models used for upscaling (**LMU** models).

3.2.3. *Upscaling of hydraulic conductivity data*

In this work, a numerical procedure of upscaling based on the advective transport equation (Eq. (1)), and particle tracking is also developed and applied, which gives an equivalent hydraulic conductivity tensor as result. The rationale to do this is to check if the hydraulic conductivities obtained by upscaling in-situ measurements match those obtained independently by numerical model calibration on hydrologic data. The upscaling has been done by using advective velocity and inverting for hydraulic conductivity to account for the complex topology of deformation bands network and diagenetic nodules distribution.

Advection is the process by which a moving fluid (i.e., groundwater) carries with it dissolved solutes (Fetter, 2018). The advective groundwater velocity can be determined from Darcy's law as

$$\boldsymbol{v} = -\frac{\boldsymbol{K}}{n_e}\nabla h \tag{1}$$

where:

$\boldsymbol{v}$ = advective velocity [L/T]
$\boldsymbol{K}$ = hydraulic conductivity tensor [L/T]
n_e = effective porosity [-]
∇h = hydraulic gradient [-]

Contaminants moving by advection, are traveling at the same rate as the average linear velocity of the ground water (Fetter, 2018).

Once obtained the flow model from MODFLOW, particle tracking was carried out with MODPATH, which requires output files from MODFLOW simulations to compute paths for imaginary particles of water (or conservative pollutants) moving throughout the system (Pollock, 2016). The path of a particle is tracked based on the components of the velocity vector at each point of the flow field. When starting the simulation, MODPATH tracks particle movements in the model until they reach a stopping condition, which could be a cell where a boundary condition is applied, or the reaching of the maximum tracking time (Pérez-Illanes and Fernàndez-Garcia, 2023). The tracking time is the accumulated time during a particle-tracking analysis (Pollock, 2016).

MODPATH allows three types of simulations, which record different information into specific output files. These are endpoints, pathlines (i.e., flow lines), and time-series simulations; pathlines were used for the upscaling process. The methodology is based on the construction of a 3-D model (**LMU**) with a volume equal to the cell size used for the regional model, in this case 10 × 10 × 500 m. This volume is then populated by structural and diagenetic structures observed in the field within the same rock volume. For this purpose, objects such as polylines for CSBs, and polygons for nodules, were drawn directly onto the model volume. Representative **LMU** models at the location of the transects or in areas

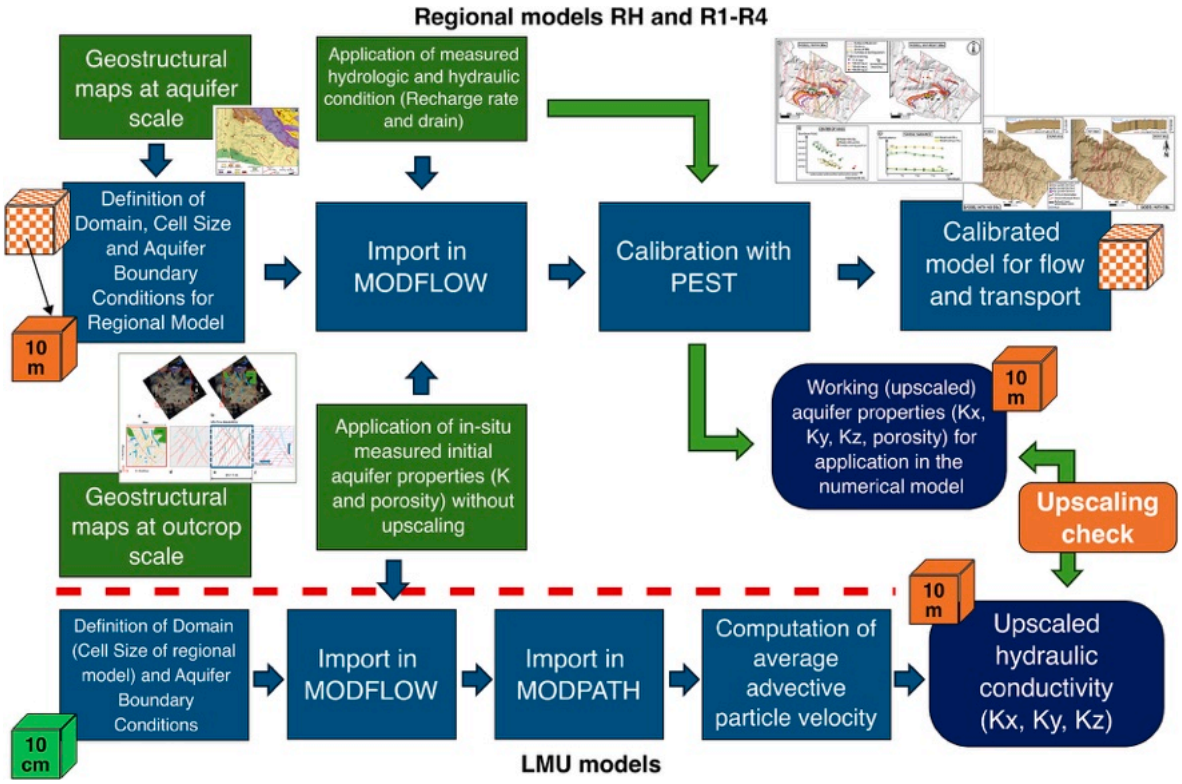

Fig. 4. Schematic diagram showing the methodological workflow followed in the numerical modeling.

Table 1
Input data for the simulations (data from Del Sole et al., 2020a).

	Permeability (mD)	Hydraulic Conductivity (m/d)
Nodule	0.03	0.025
CSBs	$K_X = 0.04$	$K_X = 0.033$
	K_Y=K_Z= 0.22	K_Y=K_Z= 0.18
Host rock	42	35

mapped in detail were considered. The method consisted of two flow simulations for each **LMU** model to generate each time flow in the X-direction (Easting) and in the Y-direction (Northing) of the flow domain in a way to compute K_x and K_y (see Fig. 9 for workflow explanation). To do this, during each simulation, constant-head boundaries were applied at two opposite sides of the model whereas the other two remained as no-flow boundaries, depending on the imposed flow direction. These boundary conditions generated a hydraulic drop (*dh)* of 1 m, chosen on the base of the model dimensions. At each simulation, particles were applied at one side of the model to trace their path towards the opposite

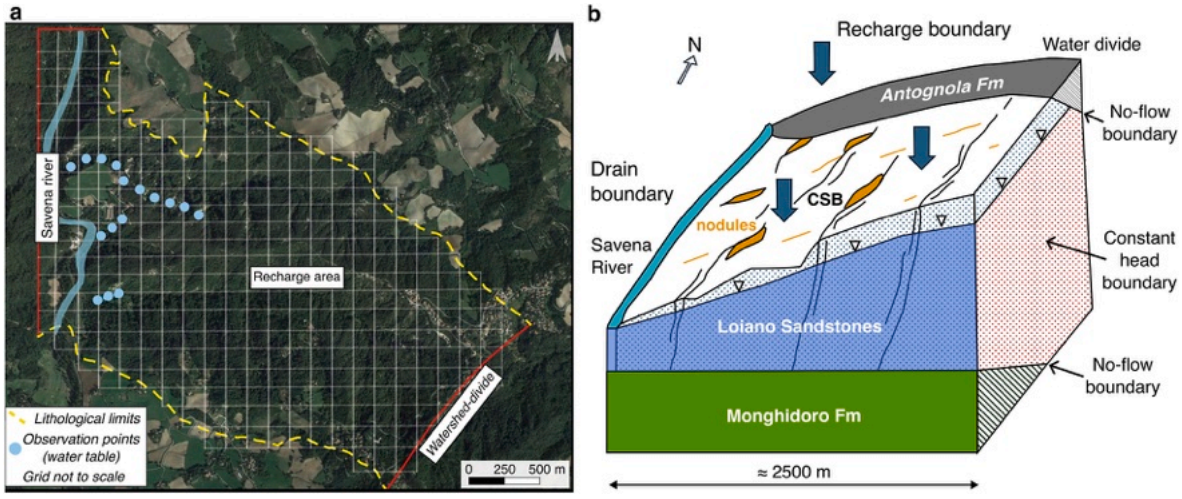

Fig. 5. (a) ©Google Earth image reporting the extent of the numerical model domain, and the boundary conditions applied. The watershed (red line) and the contacts between the Monghidoro and Anconella Fms are considered impermeable boundaries. The Savena River, on the other hand, is considered a drain boundary condition. Recharge boundary conditions are applied at the top of the model. The model is shown by the grid superposed onto the image. (b) Three-dimensional representation of the Loiano Sandstones aquifer with the boundary conditions applied. (For interpretation of the references to colour in this figure legend, the reader is referred to the Web version of this article.)

side (i.e., pathlines).

Hydraulic conductivity values for CSBs, nodules, and host rock, were taken from the study of Del Sole et al. (2020a), in which the petrophysical properties of these structures were measured *in-situ* using a mini-permeameter (Table 1). In particular, we have chosen to import into the numerical models the lower values of air permeability to avoid those data that at the outcrop surface might have been biased by poor sealing due to surface roughness. For the effective porosity, percentages of 20 %, 10 % and 6 % were chosen respectively for host rock, nodule, and CSBs.

After running the models, pathlines output files were generated, in which the time taken for the particles to reach the opposite sides of the model with respect to their starting position, was recorded. Considering the velocity term of equation (1) as:

$$v = \frac{s}{t} \tag{2}$$

where s is the space travelled by the particles (i.e. the length of the model) and t, the arrival time of each particle, the general inverse equation for the K horizontal components, K_x and K_y, respectively in the X- and Y- directions, is the following:

$$K_{i,x,y} = \frac{L^2\, n_e}{t_i\, d\mathrm{h}} \tag{3}$$

where:

$K_{i,x,y}$ = hydraulic conductivity based on the i-th particle's arrival time

L = length of the model (considered a square in this formulation)

n_e = effective porosity of the host rock

t_i = arrival time of the i-th particle

Finally, the arithmetic means of K_{ix} , and K_{iy} was calculated as follows:

$$\overline{K_x} = \frac{1}{n}\sum_{i=1}^{n}\frac{L^2\, n_e}{t_i\, d\mathrm{h}} \tag{4}$$

$$\overline{K_y} = \frac{1}{n}\sum_{i=1}^{n}\frac{L^2\, n_e}{t_i\, d\mathrm{h}} \tag{5}$$

The average hydraulic conductivity in the vertical direction ($\overline{K_z}$) was computed by using a harmonic mean of the hydraulic conductivity measured on the lithologic units mapped in the stratigraphic section of the Loiano Fm published by Del Sole et al. (2020a) and those reported in the lithologic log of the well *Sasso Marconi 1* [sasso_marconi_001.pdf (videpi.com)]. The stratigraphic section of Del Sole et al. (2020a) is 30 m long (their Fig. 10) and allows to measure the harmonic mean of hydraulic conductivity at scales ranging from 10 cm to tens of meters. The stratigraphic section in the well *Sasso Marconi 1*, on the other hand samples the whole *Loiano* Fm and it allows to compute a hydraulic conductivity at a scale of hundreds of meters. Given that the bedding is sub-horizontal and that CSBs are sub-vertical, we decided to consider only the hydraulic conductivity of the different lithological layers present in the section to compute the $\overline{K_z}$ harmonic mean:

$$\overline{K_z} = \frac{d}{\sum_{i=1}^{n}\frac{d_i}{K_i}} \tag{6}$$

Where d is the length (scale) at which the hydraulic conductivity is calculated, d_i is the thickness of the single layers (the sum of all d_i is equal to d), and K_i is the homogeneous hydraulic conductivity of each layer.

Once the three principal components of the hydraulic conductivity have been computed, we can compose the tensor for input in MODFLOW using the following form:

$$\boldsymbol{K} = \begin{bmatrix} \overline{K_x} & 0 & 0 \\ 0 & \overline{K_y} & 0 \\ 0 & 0 & \overline{K_z} \end{bmatrix} \tag{7}$$

3.2.4. Particle tracking for dispersion analysis

The application of particle tracking was also used to investigate the influence of CSBs plus nodules on particle dispersion at macroscale due to the interaction between advective velocity and heterogeneities in hydraulic conductivity.

To inject particles, new regional model objects (**RH** and **R2**) were created from which a fixed number of particles per cell was allowed to move (the total number of particles was 2549). This was a polygon object applied at the center of the models where the topography was higher (watershed divide), To investigate fluid dispersion through particle tracking, endpoint transient simulations were carried out. A certain number of tracking times (i.e., accumulated time for each experiment) were used, and each simulation stopped when it reached the specified time. In addition, steady-state simulations were carried out for pathlines tracking, in which particles stopped when they reached sink cells (i.e., drain cells).

At the end of all simulations, MODPATH recorded information of the initial and final locations of particles in an endpoint file, and the particles pathway, based on the velocity field, in a pathline file. Using the spatial coordinates, it was possible to calculate particle dispersion throughout the model after each step, both in presence and in absence of CSBs.

In fact, in a flow field with nonuniform velocity, fluid particles will tend to spread (Hsieh, 2001; Zheng, 2002). The degree of dispersion was investigated through the concept of spatial variance (in the x- and y-directions) of particle positions, defined as:

$$S_{xx} = \frac{1}{N}\sum_{1=0}^{N}(x_i - x_c)^2 \tag{8}$$

$$S_{yy} = \frac{1}{N}\sum_{1=0}^{N}(y_i - y_c)^2 \tag{9}$$

where N is the total number of particles (fluid or conservative pollutant), x_i and y_i are the x and y coordinates of the i-th particle, and x_c and y_c represent the coordinates of the center of mass, that are defined as:

$$x_c = \frac{1}{N}\sum_{1=0}^{N}x_i \tag{10}$$

$$y_c = \frac{1}{N}\sum_{1=0}^{N}y_i \tag{11}$$

The center of mass in our case represents the mean location of a distribution of mass in space. The center of mass calculated for each time step revealed the average trajectory of the particle cloud.

Particles position and the center of mass at each time step were then imported into a map associated with a DEM (digital elevation model), to determine the movement of particles, their dispersion, and to check if there was a topographic control on the process.

4. Results

4.1. Field work

Fig. 6a shows the structural map of major CSBs zones and the statistical analysis of azimuth data for all CSBs in the study area (Fig. 6b, c) whereas Figs. S1, S2, and S3 in Supplementary Material show data subdivided into transects. In Fig. 6b, c orientation data are reported as dip azimuth angles and they are subdivided into CSBs associated with nodules and CSBs not associated with nodules. The dip azimuth

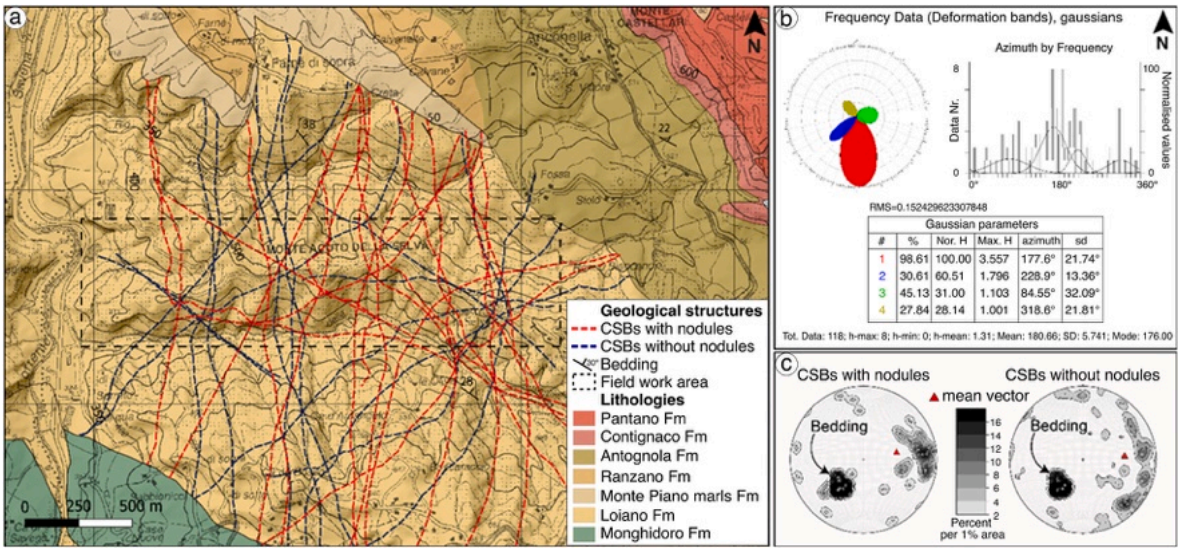

Fig. 6. Structural data in study area. (a) Traces of CSB zones (at least 10 individual CSBs). (b) Frequency azimuth distribution for CSBs. (c) Equal area stereographic projection for CSBs azimuth, which are associated (on the left) and not associated (on the right) with the carbonate nodules. Pole to bedding is also reported.

frequency rose diagram of all CSBs data is presented in Fig. 6b, whereas the poles to principal directions of CSBs, subdivided based on the presence or not of nodules, are reported into lower hemisphere equal area projections (Fig. 6c). In the latter, also bedding data are presented. CSBs fall into 4 main sets, showing dip azimuth SSE, SSW, ENE, NNW. Frequency data analysis indicates that the most represented set is the SSE-dipping one, although characterized by a certain variability (i.e., standard deviation of 21°). The mean dip azimuth of all CSBs data is 180°, which means an E-W–oriented strike. The major continuous CSB zones have a N-S strike (Fig. 6a).

Field observations show that the length of CSBs ranges typically from 1 m to 600 m. The thickness of a single CSB ranges typically from 2 to 5 mm. Zones where up to tens of CSBs are subparallel and close to one another form a tabular structure with thickness of a few centimeters. They may have an anastomosing pattern in three dimensions, characterized by variable directions along their length, but also branching and merging of two or more fault strands.

A single CSB accommodates typically an offset of a few millimeters, whereas CSB zones consisting of 5–30 CSBs may accommodate an offset of up to a few centimeters. Observed offsets for CSBs zones in the study area ranged from 10 to 15 cm. Carbonate nodules are variable in size, ranging from less than 15 cm in diameter to tens of meters in length for the tabular concretions. The latter show thickness ranging from 15 cm up to 1 m.

The trend of the mean pole or mean vector to CSBs with nodules is 087° and has a plunge of 49°, whereas the trend of the mean pole to CSBs not associated with nodules is 089° and a plunge of 41° (Fig. 6c). In both stereoplots, bedding azimuth is dipping ENE of 10–15°.

The surface water level measured in creeks as a function of distance from the River Savena (see Fig. 4.4b for location of calibration points) is shown in Fig. 7. Data were interpolated and reported in an E-W cross section; $R^2 = 0{,}946$ of the interpolation).

4.2. Calibration of the regional numerical flow model

The groundwater head distribution for the regional model **RH** was created by modeling the domain with a homogeneous *K* and boundary conditions of recharge on top, no flow on three sides and a drain on the eastern end (Fig. 8a and 5b). Fig. 8b, on the other hand, shows the head distribution for the regional model (**R2**) that simulates an inhomogeneous K due to the presence of the CSBs and nodules.

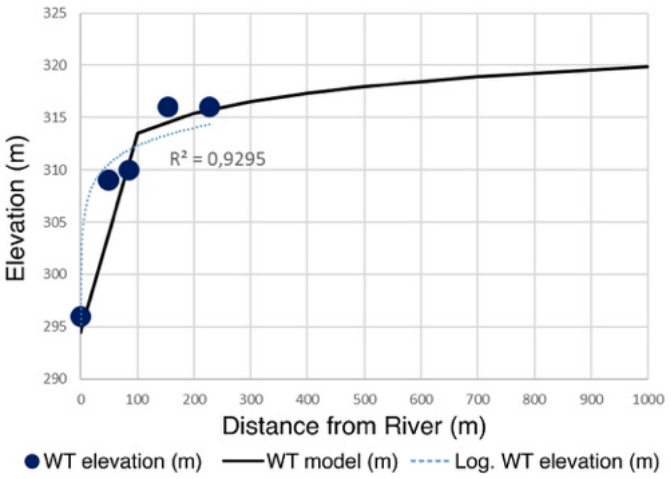

Fig. 7. Comparison between water table elevation obtained in numerical models (solid black line), water table elevation measured in the field (solid blue dots), and water table interpolated from the field data (Log-WT thin dashed light blue line). (For interpretation of the references to colour in this figure legend, the reader is referred to the Web version of this article.)

PEST sensitivity in calibration was tested by trying different combinations of K in the **R1-4** models reported in Tables 2 and 3. This was done to check what PEST-derived K values were more realistic in view of what measured *in-situ*. In Case **R1**, both CSBs and matrix hydraulic conductivity were allowed to be adjusted by the program, and initial values were taken from literature Table 1. In this case, given an initial value of 35 m/d for the matrix and 0.4 m/d for CSBs, the results were, respectively, 31.67 m/d and 0.55 m/d.

In Case **R2**, Case **R3** and Case **R4**, the K of the matrix was kept constant, while allowing the program to change the hydraulic conductivity of the CSBs. In Case **R2** and Case **R3**, the K of the matrix was equal to a fixed value of 35 m/d, whereas that of CSBs was, respectively, 15 m/d and 30 m/d. Although K was allowed to vary within five orders of magnitude, calibration gave as result K_{CSB} values of 0.37 m/d for Case **R2** and 0.46 for Case **R3**. Finally, for Case **R4** it was decided to increase the matrix input K up to 100 m/d, maintaining it fixed during simulation, and a K_{CSBs} equal to 10 m/d; the result for K_{CSB} was 1 m/d.

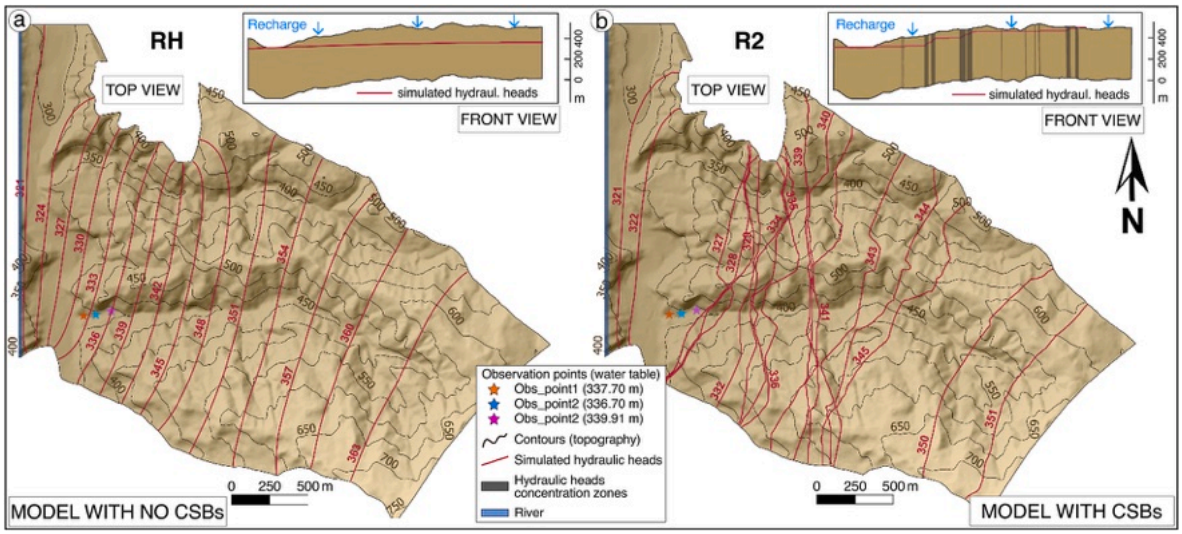

Fig. 8. Water table maps from MODFLOW numerical experiments in the case of a homogeneous sandstone aquifer (a) and of an aquifer including structural heterogeneities such as the CSBs. The hydraulic head distribution is represented by the red contour lines, whereas the black contour lines represent topography. (For interpretation of the references to colour in this figure legend, the reader is referred to the Web version of this article.)

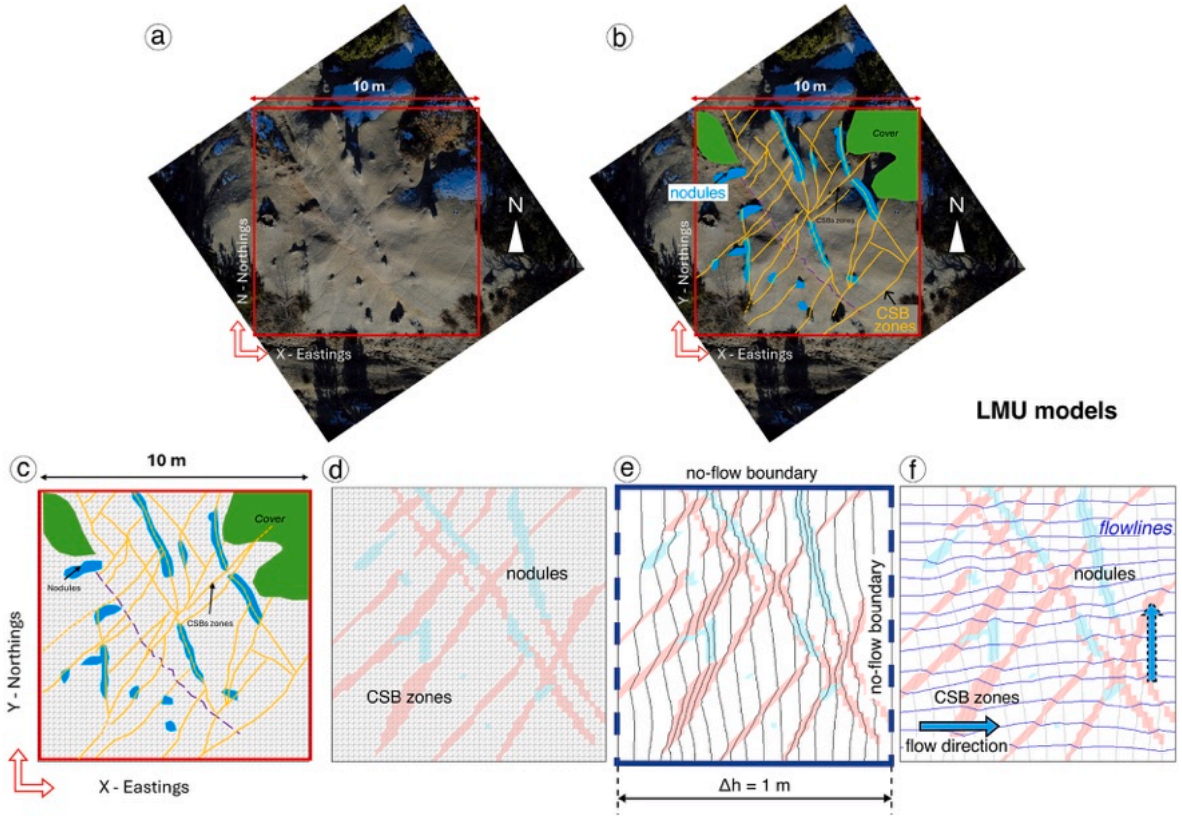

Fig. 9. (a) Figure showing typical measurements made for several outcrops at the meter-scale by mapping and upscaling. Inclusion of heterogeneities (CSBs) in hydraulic conductivity is shown in the construction of aquifer model cell size 10 × 10 × 500 m. (b) Map of the outcrop showing the CSBs zones and the nodules. (c) Import of the map into the numerical model. (d) Petrophysical properties definition on cells of the model. (e) Solution of the model showing the boundary conditions of the model computing flow in the X-direction (solid blue lines) and in the Y-direction (dashed blue lines). Equipotential lines (grey lines) are also shown. (f) Pathlines computation and their travel time in the X-direction and in the Y-direction. (For interpretation of the references to colour in this figure legend, the reader is referred to the Web version of this article.)

Although the K of the matrix was increased, CSBs showed again hydraulic conductivity two orders of magnitude lower than that of the matrix.

The errors between the measured hydraulic head and the simulated hydraulic head (**R** models) are the following: mean error = 0.01 m; mean absolute error = 2.001 m; RMS (Root mean square) Error = 0.036 m. All discrepancy values were negative, meaning that the calculated water budget indicated more water leaving the model with respect to

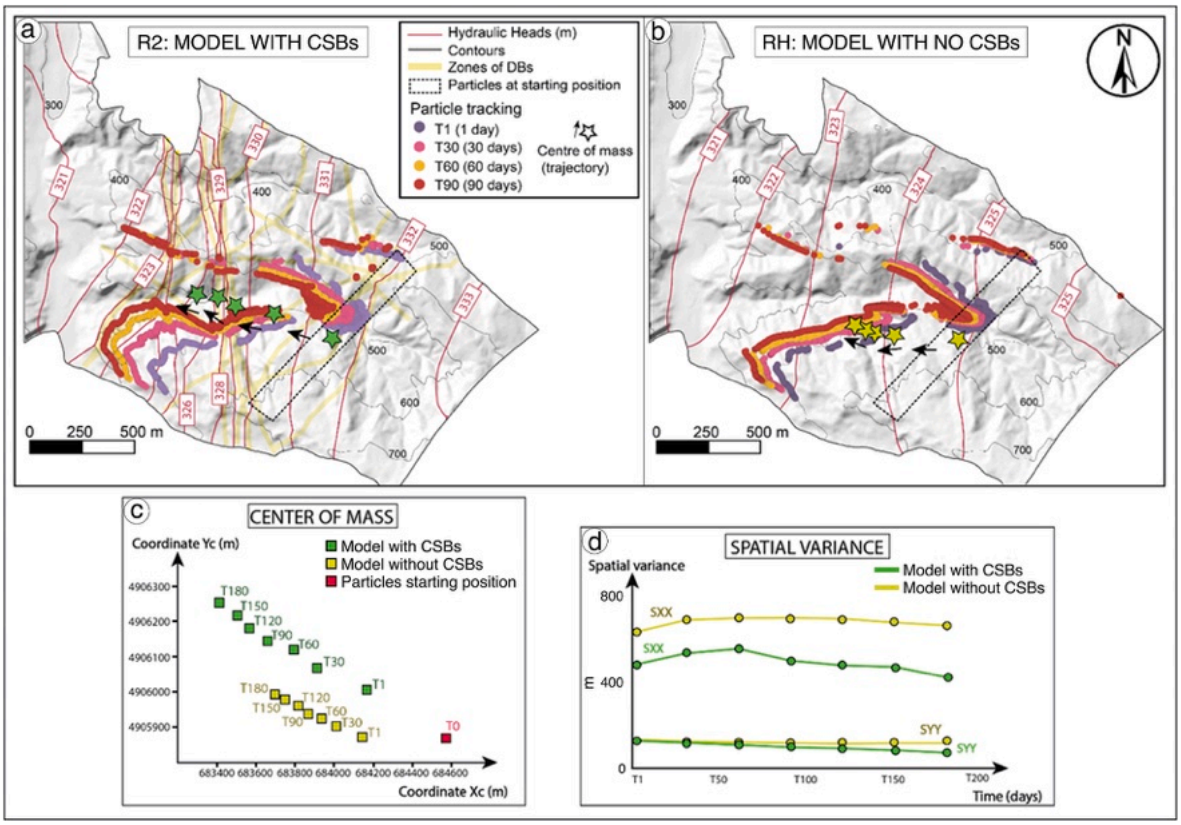

Fig. 10. (a, b) Map view of the particle fronts moving within the aquifer. Model with (a) and without (b) CSBs. The starting point of the particles is the rectangle along the water divide marked with a dotted line. Particle fronts are visualized after 1, 30, 60, and 90 days of simulation. The stars indicate the center of mass for the particles. The red contour lines indicate the hydraulic head. (c) Movement of the center of mass for the particles in the two models. The time zero initial position for all particles is at the red square (T0); the position of the center of mass is given for both models at 1, 30, 60, 90, 120, 150 and 180 days. (d) Spatial variance of the particles with respect to the center of mass in the X-direction (S_{XX}) and in the Y-direction (S_{YY}). (For interpretation of the references to colour in this figure legend, the reader is referred to the Web version of this article.)

that entering. Only values of discrepancy lower than 1 (a stringent default value), were accepted for the convergence criteria in all models presented.

4.3. Upscaling of hydraulic conductivity data

Simulations (**LMU** models) with realistic geometry of CSBs were carried out to obtain K values at the scale of the individual cells (Fig. 9) of the regional numerical models (**R**). Outcrop images showing the arrangement of CSBs (yellow lines) and nodules (light blue polygons) in the outcrops are shown in Fig. 9a and b. Fig. 9c shows how the shapefile of CSBs (polylines) and carbonate nodules (polygons) are imported into a 10 × 10 × 500 m domain cell discretized on a grid with a 0.1 m side and the petrophysical properties are assigned to the grid (Fig. 9d). Particle pathlines (flowlines) are computed in the X-direction to evaluate K_x and in the Y-direction to evaluate K_y by rotating 90° the boundary conditions (solid blue line X-direction flow; dashed blue lines Y-direction flow in Fig. 9e and f.

Fig. 9 shows an **LMU** model with a 10 × 10 × 500 m domain and 10 cm side cells. The resulting equivalent (at domain scale in Fig. 9) hydraulic conductivity component K_x is equal to 0.7 m/d, and the component K_y is equal to 0.9 m/d. These are average values that we have obtained by computation in other **LMU**s models at the location of transects 1, 2, 3, 4, 5, 6, and 7.

Table 3 summarizes all data obtained for the three hydraulic components K_x, K_y, and K_z and the relative scales in the **LMU** models.

4.4. Particle tracking analysis

Particle tracking analysis, based on particle tracking movement by advective velocity, is presented in Fig. 10. Comparing the model with (**RH**; Fig. 10a) and without CSBs (**R2**; Fig. 10 b), we can say that particles underwent less dispersion, both in the Y-direction (i.e., northing direction) and the X-direction (i.e., easting direction), where CSBs were present (**R2**); they were also faster and reached longer distances (Fig. 10a). On the contrary, in the model without CSBs (**RH**), particles moved slower, they had more dispersion in the X- and Y- directions and travelled shorter distances (Fig. 10b). The higher particle velocity in the model with CSBs is clear in the graph of Fig. 10c. In fact, at the same time step, the center of mass for the particles in the CSBs **R2** model (green points) has moved further from the initial starting position than the center of mass for the particles in the **RH** model without CSBs (yellow points). The center of mass of the green particles has moved further both in the X- and Y-coordinates with respect to the center of mass of the yellow particles. In addition, particles followed two different paths across the two models; the particles in the **R2** model followed a more northerly route (Fig. 10a) whereas those in the **RH** model followed a more southerly route (Fig. 10b). This is because particles in the model without CSBs are steered only by the topographic gradient, whereas in the model with CSBs, particles are driven also by the orientation of the CSBs in space.

Spatial variance results are divided into variance distributions in X- and Y- directions (Fig. 10d). The spatial variance in both directions (S_{xx} and S_{yy}) has higher values (average 700 m for S_{xx} and 100 m for S_{yy}) in the model without CSBs than the one with CSBs (average 500 m for S_{xx} and 90 m for S_{yy}). Where CSBs are not present, however, the variance

Table 2
Manual calibration parameters. The best (less discrepancy) values for matrix hydraulic conductivity are 0.2–0.3 m/d.

Manual Calibration (model with no CSBs) – RH					
K matrix (m/d)		Discrepancy %		Residuals (m)	
35		−156			
				17.83	
10		−23.7			
				17.66	
1		−1.35			
				13.87	
0.9		−0.5			
				13.4	
0.8		−0.27			
				12.82	
0.7		−0.46			
				12.07	
0.5		−0.51			
				9.7	
0.3		−0.43			
				4.24	
0.2		−0.49			
				3.03	
Automatic calibration (model with no CSBs)					
	Input K (m/d)	**PEST parameters**	**Range of variation**	**Estimated K (m/d)**	**Ratio K matrix/K DBs**
Case 1 – R1					
Matrix	35	K_{matrix}	1.1–10	31.67	58
DBs	0.4	K_{CSBs}	1E-5 – 10	0.55	
Case 2 - R2					
Matrix	35	Fixed	n/a	35	95
DBs	15	K_{CSBs}	1E-4 – 10	0.37	
Case 3 – R3					
Matrix	35	Fixed	n/a	35	76
DBs	30	K_{CSBs}	1E-4 – 10	0.46	
Case 4 – R4					
Matrix	100	Fixed	n/a	100	100
DBs	10	K_{CSBs}	1E-4 – 10	1	

has a constant trend in time, meaning that particles moved uniformly across the area, keeping the same distances relative to each other and to the center of mass. In the case of the model with CSBs, the variance in Y-direction has a linear decreasing trend, whereas that in the X-direction is more irregular, with a decreasing trend (Fig. 10d).

5. Discussion

One of the novelties of our approach in studying the effects of structural and diagenetic heterogeneities on saturated single phase fluid flow in an aquifer within porous sandstones has been the calibration with field measured water level data and boundary conditions.

The calibrated homogenous and isotropic model for the regional Loiano Sandstone aquifer (**RH**) produces the best fit between computed and measured data for a hydraulic conductivity $K_x = K_y = K_z = 0.2–0.3$ m/d, which is much less than the hydraulic conductivity of the Loiano Sandstone matrix (35 m/d). This means that the presence of lithological, structural, and diagenetic heterogeneities has decreased the equivalent permeability of the aquifer of two orders of magnitude with respect to the host rock. As this result is in line with other numerical modeling studies (Zuluaga et al., 2016; Souza et al., 2022; Berge et al., 2022), it is interesting to note that an isotropic K fits well the field water level data. This result may be since the CSB sets strike at almost 90° from each other. In addition, the topographically driven flow in the Loiano aquifer may also be influenced by the low average vertical hydraulic conductivity ($K_z \approx 0.1$ m/d). A similar effect has also been observed recently by Sutton and Zahasky (2025) when implementing small scale fracturing in models of core size samples.

The other important objective of our study was to develop and test an upscaling methodology that can be easily implemented by starting with structural and petrophysical data collected at the scale of the outcrop (detailed maps scale 1:10 to 1:100, *in-situ* permeability measurements, porosity determinations from hand-size collected samples, etc.) with the open source numerical flow model and advective transport simulators MODFLOW and MODPATH. The use of open-source software with respect to proprietary software as often reported in the literature (see Zuluaga et al., 2016; Berge et al., 2022) makes the methodology available to a wide number of researchers both involved in the study of aquifers or any other type of geofluids modeling.

Upscaling is necessary to implement in flow simulators the effect of fine-scale geological structures such as CSBs and carbonate nodules, because of the prohibitively high discretization of the individual cells that would be necessary in the simulator grid to account of these features and that would lead to expensive computational costs. The first attempts to upscale permeability from the scale of the CSBs to that of the cells within a reservoir were done by Antonellini and Aydin (1995) and by Matthäi et al. (1998) who used an equivalent permeability model for

Table 3
Modeling results.

Model scale		Model domain (m)	Cell size (m)	K_x (m/d)	K_y (m/d)	K_z (m/d)	Khr (m/d)	K_z SM (960 m) (m/d)	K_z LOI log (30 m) (m/d)	K model with PEST calibration (m/d)
Regional isotropic - **RH**	Manual calibration	4000 × 1800 × 400	10 × 10xZ Z = Top LOI – Bottom LOI ≈ 400 m	0.2–0.3	0.2–0.3	0.2–0.3				
Regional with CSBs **Case 1 -R1**	PEST calibration	4000 × 1800 × 400	10 × 10xZ				31.67			0.55
Regional with CSBs **Case 2 – R2**	PEST calibration	4000 × 1800 × 400	10 × 10xZ				35 fixed			0.37
Regional with CSBs **Case 3 – R3**	PEST calibration	4000 × 1800 × 400	10 × 10xZ				35 fixed			0.46
Regional with CSBs **Case 4 – R4**	PEST calibration	4000 × 1800 × 400	10 × 10xZ				100 fixed			1
Outcrop box - **LMU**	1 set CSB	10 × 10 × 400	0.1 × 0.1 × 0.1	0.7	25.8			0.1	0.23	
Outcrop box - **LMU**	Tabular carbonate nodule	10 × 10 × 400	0.1 × 0.1 × 0.1	0.11	19.06			0.1	0.23	
Outcrop box - **LMU**	2 sets of CSB and carbonate nodules	10 × 10 × 400	0.1 × 0.1 × 0.1	0.7	0.9			0.1	0.23	

including the permeability of CSBs and slip surfaces measured at cm-scale to a scale of a block of 1-m to tens of meters scale. The equivalent permeability was computed by harmonic average for the flow normal to the structural heterogeneities and by arithmetic average for the flow parallel to the heterogeneities (Antonellini and Aydin, 1994, 1995). Other authors explored further this upscaling methodology also testing its sensitivity in large scale simulations and implementing the geometric characteristics of the CSBs (see Rotevatn et al., 2013 and literature therein).

Zuluaga et al. (2016) followed a different approach in upscaling DBs permeability to reservoir scale by using a methodology initially published by Durlofsky (1991, 2005) for upscaling and gridding of fine-scale geological models for flow simulation in fractured reservoirs. The method consists in assigning a unit drop in pressure across the DBs and computing its permeability by knowing the flow rate through the cell. This methodology, however, cannot account for the fine scale topology of the DBs network.

In our upscaling methodology, we can implement the fine scale structure of deformation bands and carbonate nodules at the cm-scale. Furthermore, using an outcrop box (**LMU**) with an area of 10 × 10 m it allows to capture the changes along strike of the zones of CSBs and of the nodules, their eventual termination within the box, the presence of steps across which the flow may easily occur, and/or their interaction with differently oriented sets. Another novelty in our upscaling methodology is to use the advective velocity to obtain hydraulic conductivity via experiments on individual reservoir cells (10 × 10 × 500 m). These reservoir cells contain the exact geometry and location of the CSBs and carbonate nodules in the outcrops mapped. The equivalent hydraulic conductivities obtained in the different cells can then be assigned in the regional models (**R** models). To decrease the computational time and to put more emphasis on the high dip angle structural heterogeneities, which are prevalent in the outcrop studied, the vertical hydraulic conductivity was upscaled by harmonic averaging using the stratigraphic logs available (Del Sole et al., 2020a and videpi.com).

The validity of the upscaling methodology is tested using the results of the calibrated numerical models (**RH** and **R1-4**). By comparing the K obtained for the calibrated isotropic regional model **RH** ($K_x = K_y = K_z =$ 0.2–0.3 m/d) and the calibrated regional models with structural heterogeneities **R1-4** (K_{CSB} = 0.37–0.55 m/d) with the results of outcrop upscaling (**LMU** - K_x = 0.11–0.7 m/d, K_y = 0.9–25.8 m/d, and K_z = 0.1–0.23), we conclude that these latter are in good agreement with K obtained from model calibration.

The possibility of having calibrated flow models offered us the opportunity to explore also the effects of CSBs on mass transport in saturated flow within a porous aquifer. In the models that we present in Fig. 10, the effects of CSBs and nodules on advective velocity and dispersion of conservative pollutants within an aquifer are rather interesting. Confronting the regional isotropic model (**RH**) with the regional model including the CSBs (**R1-4**), in fact, shows that the models with CSBs increase the advective velocity and decrease the dispersion in x (S_{xx}) with respect to the model without CSBs. Despite being the two models similar in terms of flow, they are not in terms of mass transport. The higher K in the host rock of the model with CSBs (**R2**) helps keep advective velocity high with respect to the model without CSBs (**RH**). This has important implications, because the advective velocity of pollutants in an aquifer with CSBs where the K has been implemented at the scale of the structures and therefore is closer to reality, move faster than in a model where an equivalent homogeneous K has been adopted (Fig. 10a–c). Dispersion, at least in the X-direction, is more pronounced in the **RH** model than in the **R2** one. This could be due to the topographic effect that is more pronounced under slow advective velocity or to the containment effect of CSBs on advective flow. This, however, is something that needs to be investigated further.

The numerical methodologies that we have used could be further improved by using a more detailed vertical stratigraphic description of the aquifer and the implementation of heterogeneities in hydraulic K due to bed-parallel carbonate nodules, as well as the implementation of three-dimensional nodules geometries. Furthermore, the seasonal variability of recharge could be implemented to obtain a calibration at finer temporal scale. All this, of course, comes with a computational cost that, on the other hand, may become feasible soon.

6. Conclusions

The results that we have obtained are important because they show a practical approach to the upscaling problem, especially where there are large differences in scale between the size of the heterogeneities and the size of the numerical model cells. This is important for hydrogeological characterization of aquifers and the management of their resources. Similarly, the methodology could be applied as an outcrop analog for reservoir modeling of any geofluid in the subsurface and may be beneficial for a spectrum of environmental issues and industrial operations (e.g., geologic CO_2 sequestration, waste fluid disposal, groundwater contaminant transport and remediation; energy appraisal). The novelty of our work is that, to the best of our knowledge, for the first time we try a calibration of the model with data collected in the field in the contest of heterogeneities due to deformation and diagenesis in porous sandstones.

The major findings of our work may be summarized as follows.

i. The presence of diagenetic (carbonate nodules) and structural heterogeneities in a porous sandstone aquifer may decrease 2-3 orders of magnitude the hydraulic conductivity of the pristine host rock. The result of our calibrated model is in line with other results from the literature that, however, were not calibrated with field data.
ii. The upscaling methodology for hydraulic conductivity that allows inclusion of structures and diagenetic features measured at the outcrop-scale by means of inversion of the advective velocity of conservative particles has been successfully validated by comparison with results of the calibrated model. This methodology, therefore, could be used for easily implementing field data in aquifers or other geofluids (e.g., Hydrocarbons, H_2, CO_2) reservoir simulators.
iii. Structural and diagenetic heterogeneities effects on mass transport are for the first time explored. From our experiments, the use of an equivalent isotropic hydraulic conductivity approach fails to correctly account for mass transport in porous sandstone aquifers both in terms of advective velocity and dispersion. Our recommendation is to implement, as much as possible the local heterogeneities in K within the model to obtain a more realistic and conservative estimate of advection and dispersion.

Our findings should be helpful to all those geoscientists that are trying to include more of the real geologic world in numerical simulations. Our methodology is robust and will be further extended by including a more detailed account of the stratigraphy of the aquifer and of how the properties of the CSBs may change from one layer to the other according to variation in clay content, sorting, and carbonate cement precipitation properties that, so far, are not yet included but are important for the refinement of the hydraulic conductivity values used in numerical simulations.

CRediT authorship contribution statement

Marco Antonellini: Writing – review & editing, Writing – original draft, Visualization, Validation, Supervision, Software, Resources, Project administration, Methodology, Investigation, Funding acquisition, Formal analysis, Data curation, Conceptualization. **Leonardo Del Sole:** Writing – review & editing, Writing – original draft, Visualization, Validation, Methodology, Investigation, Data curation. **Pauline Nella Mollema:** Writing – review & editing, Writing – original draft,

Validation.

Declaration of competing interest

The authors declare that they have no known competing financial interests or personal relationships that could have appeared to influence the work reported in this paper.

Acknowledgments

This study has been possible thanks to funding for basic research of the authors institution (Alma Mater Studiorum – Università di Bologna). The authors wish to thank the Structural Geology & Tectonics Division of the Geological Society of America (GSA) for the 2020 'Stephen E. Laubach Structural Diagenesis Research Award' given to L. Del Sole. Sabrina Napoleoni is acknowledged for help in data collection. We would like to thank the two anonymous reviewers for their valuable feedback, which helped enhance the clarity of this work.

Appendix A. Supplementary data

Supplementary data to this article can be found online at https://doi.org/10.1016/j.marpetgeo.2025.107406.

Data availability

Data will be made available on request.

References

Ahlfeld, D.P., Hoque, Y., 2008. Impact of simulation model solver performance on ground water management problems. Groundwater 46, 716–726. https://doi.org/10.1111/j.1745-6584.2008.00454.x.

Antonellini, M., Aydin, A., 1994. Effect of faulting on fluid flow in porous sandstones: petrophysical properties. American Association of Petroleum Geologists Bulletin 78, 355–377. https://doi.org/10.1306/BDFF90AA-1718-11D7-8645000102C1865D.

Antonellini, M., Aydin, A., 1995. Effect of faulting on fluid flow in porous sandstones: geometry and spatial distribution. American Association of Petroleum Geologists Bulletin 79, 642–671. https://doi.org/10.1306/8D2B1B60-171E-11D7-8645000102C1865D.

Antonellini, M., Aydin, A., Orr, L., 1999. Outcrop-aided characterization of a faulted hydrocarbon reservoir: Arroyo grande oil field, California, USA. In: Haneberg, W.C., Mozley, P.S., Moore, J.C., Goodwin, L.B. (Eds.), Faults and Subsurface Fluid Flow in the Shallow Crust, vol. 113. American Geophysical Union, Geophysical Monograph, Washington DC, USA, pp. 7–26. https://doi.org/10.1029/GM113p0007.

Antonellini, M., Aydin, A., Pollard, D.D., D'Onfro, P., 1994. Petrophysical study of faults in sandstone using petrographic image analysis and X-ray computerized tomography. Pure and Applied Geophysics PAGEOPH 143, 181–201. https://doi.org/10.1007/BF00874328.

Antonellini, M., Cilona, A., Tondi, E., Zambrano, M., Agosta, F., 2014. Fluid flow numerical experiments of faulted porous carbonates, northwest sicily (Italy). Mar. Petrol. Geol. 55, 186–201. https://doi.org/10.1016/j.marpetgeo.2013.12.003.

Antonellini, M., Mollema, P.N., 2002. Cataclastic faults in the Loiano sandstones; Northern apennines, Italy. Boll. Soc. Geol. It. 121, 163–178. https://www.socgeol.info/it/fascicoli/?t=Bollettino&y=2002&v=121.

Awdal, A., Suramairy, R., Singh, K., Fabre, G., Alsop, G.I., 2020. Deformation bands and their impact on fluid flow: insights from geometrical modelling and multi-scale flow simulations in sandstones. J. Struct. Geol. 141, 104215. https://doi.org/10.1016/j.jsg.2020.104215.

Aydin, A., 2000. Fractures, faults, hydrocarbon entrapment, migration, and flow. Mar. Petrol. Geol. 17, 797–814. https://doi.org/10.1016/S0264-8172(00)00020-9.

Aydin, A., Borja, R.I., Eichhubl, P., 2006. Geological and mathematical framework for failure modes in granular rock. J. Struct. Geol. 28, 83–98. https://doi.org/10.1016/j.jsg.2005.07.008.

Aydin, A., Ahmadov, R., Antonellini, M., Cherry, J., Cilona, A., Deng, S., Flodin, E., de Joussineau, G., Parker, B., Zhong, J., 2023. Fractures and faults in sandstone and sandstone-Shale/Mudstone sequences and their impact on groundwater. The Groundwater Project. https://doi.org/10.21083/978-1-77470-012-9.

Aydin, A., Johnson, A.M., 1978. Development of faults as zones of deformation bands and as slip surfaces in sandstone. PAGEOPH 116, 931–942. https://doi.org/10.1007/BF00876547.

Ballas, G., Fossen, H., Soliva, R., 2015. Factors controlling permeability of cataclastic deformation bands and faults in porous sandstone reservoirs. J. Struct. Geol. 76, 1–21. https://doi.org/10.1016/j.jsg.2015.03.013.

Bense, V.F., Van den Berg, E.H., Van Balen, R.T., 2003. Deformation mechanisms and hydraulic properties of fault zones in unconsolidated sediments; the roer valley rift system, the Netherlands. Hydrogeol. J. 11, 319–332. https://doi.org/10.1007/s10040-003-0262-8.

Berge, R.L., Gasda, S.E., Keilegavlen, E., Sandve, T.H., 2022. Impact of deformation bands on fault-related fluid flow in field-scale simulations. Int. J. Greenh. Gas Control 119, 103729. https://doi.org/10.1016/j.ijggc.2022.103729.

Bettelli, G., Vannucchi, P., 2003. Structural style of the offscraped Ligurian Oceanic sequences of the northern apennines: new hypothesis concerning the development of mélange block-in-matrix fabric. J. Struct. Geol. 25, 371–388. https://doi.org/10.1016/S0191-8141(02)00026-3.

Bisdom, K., Bertotti, G., Nick, H.M., 2016a. The impact of in-situ stress and outcrop-based fracture geometry on hydraulic aperture and upscaled permeability in fractured reservoirs. Tectonophysics, The role of fluids in faulting and fracturing in carbonates and other upper crustal rocks 690, 63–75. https://doi.org/10.1016/j.tecto.2016.04.006.

Bisdom, K., Bertotti, G., Nick, H.M., 2016b. The impact of different aperture distribution models and critical stress criteria on equivalent permeability in fractured rocks. J. Geophys. Res. Solid Earth 121, 4045–4063. https://doi.org/10.1002/2015JB012657.

Boccaletti, M., Corti, G., Martelli, L., 2011. Recent and active tectonics of the external zone of the Northern Apennines (Italy). Int. J. Earth Sci. 100, 1331–1348. https://doi.org/10.1007/s00531-010-0545-y.

Boccaletti, M., Guazzone, G., 1974. Remnant arcs and marginal basins in the Cainozoic development of the Mediterranean. Nature 252, 18–21. https://doi.org/10.1038/252018a0.

Cheong, J., Hamm, S., Kim, H., Ko, E., Yang, K., Lee, J., 2008. Estimating hydraulic conductivity using grain-size analyses, aquifer tests, and numerical modeling in a riverside alluvial system in South Korea. Hydrogeol. J. 16, 1129–1143. https://doi.org/10.1007/s10040-008-0303-4.

Cibin, U., Cavazza, W., Fontana, D., Milliken, K.L., McBride, E.F., 1993. Comparison of composition and texture of calcite-cemented concretions and host sandstones, Northern Apennines, Italy. J. Sediment. Res. 63, 945–954. https://doi.org/10.1306/D4267C4E-2B26-11D7-8648000102C1865D.

Cibin, U., Spadafora, E., Zuffa, G.G., Castellarin, A., 2001. Continental collision history from arenites of episutural basins in the Northern Apennines, Italy. GSA Bulletin 113, 4–19. https://doi.org/10.1130/0016-7606(2001)113<0004:CCHFAO>2.0.CO;2.

Conti, P., Cornamusini, G., Carmignani, L., 2020. An outline of the geology of the Northern Apennines (Italy), with geological map at 1:250,000 scale. Italian Journal of Geosciences 139, 149–194. https://doi.org/10.3301/IJG.2019.25.

Conti, S., Fioroni, C., Fontana, D., Grillenzoni, C., 2016. Depositional history of the Epiligurian wedge-top basin in the Val marecchia area (northern Apennines, Italy): a revision of the Burdigalian-Tortonian succession. Italian Journal of Geosciences 135, 324–335. https://doi.org/10.3301/IJG.2015.32.

Del Sole, L., Antonellini, M., 2019. Microstructural, petrophysical, and mechanical properties of compactive shear bands associated to calcite cement concretions in arkose sandstone. J. Struct. Geol. 126, 51–68. https://doi.org/10.1016/j.jsg.2019.05.007.

Del Sole, L., Antonellini, M., Calafato, A., 2020a. Characterization of sub-seismic resolution structural diagenetic heterogeneities in porous sandstones: combining ground-penetrating radar profiles with geomechanical and petrophysical in situ measurements (Northern Apennines, Italy). Mar. Petrol. Geol. 117, 104375. https://doi.org/10.1016/j.marpetgeo.2020.104375.

Del Sole, L., Antonellini, M., Soliva, R., Ballas, G., Balsamo, F., Viola, G., 2020b. Structural control on fluid flow and shallow diagenesis: insights from calcite cementation along deformation bands in porous sandstones. Solid Earth 11, 2169–2195. https://doi.org/10.5194/se-11-2169-2020.

Dewandel, B., Maréchal, J.C., Bour, O., Ladouche, B., Ahmed, S., Chandra, S., Pauwels, H., 2012. Upscaling and regionalizing hydraulic conductivity and effective porosity at watershed scale in deeply weathered crystalline aquifers. J. Hydrol. 416, 83–97. https://doi.org/10.1016/j.jhydrol.2011.11.038.

Doherty, J., 2015. Calibration and Uncertainty Analysis for Complex Environmental Models. Watermark Numerical Computing, Brisbane, Australia, p. 227. ISBN: 978-0-9943786-0-6 Downloadable from. www.pesthomepage.org.

Du Bernard, X., Eichhubl, P., Aydin, A., 2002. Dilation bands: a new form of localized failure in granular media. Geophys. Res. Lett. 29. https://doi.org/10.1029/2002GL015966, 29-1-29–4.

Durlofsky, L.J., 1991. Numerical calculation of equivalent grid block permeability tensors for heterogeneous porous media. Water Resour. Res. 27, 699–708. https://doi.org/10.1029/91WR00107.

Durlofsky, L.J., 2005. Upscaling and gridding of fine scale geological models for flow simulation. In: 8th International Forum on Reservoir Simulation, pp. 1–59.

Edwards, H.E., Becker, A.D., Howell, J.A., 1993. Compartmentalization of an Aeolian Sandstone by Structural Heterogeneities: Permo-Triassic Hopeman Sandstone, Moray Firth, Scotland, vol. 73. Geological Society, London, Special Publications, pp. 339–365. https://doi.org/10.1144/GSL.SP.1993.073.01.20.

Fachri, M., Rotevatn, A., Tveranger, J., 2013a. Fluid flow in relay zones revisited: towards an improved representation of small-scale structural heterogeneities in flow models. Mar. Petrol. Geol. 46, 144–164. https://doi.org/10.1016/j.marpetgeo.2013.05.016.

Fachri, M., Tveranger, J., Braathen, A., Schueller, S., 2013b. Sensitivity of fluid flow to deformation-band damage zone heterogeneities: a study using fault facies and truncated gaussian simulation. J. Struct. Geol. 52, 60–79. https://doi.org/10.1016/j.jsg.2013.04.005.

Fetter, C.W., 2018. In: Applied Hydrogeology, fourth ed. Waveland Press.

Fossen, H., Bale, A., 2007. Deformation bands and their influence on fluid flow. AAPG (Am. Assoc. Pet. Geol.) Bull. 91, 1685–1700. https://doi.org/10.1306/07300706146.
Fossen, H., Schultz, R.A., Shipton, Z.K., Mair, K., 2007. Deformation bands in sandstone: a review. J. Geol. Soc. 164, 755–769. https://doi.org/10.1144/0016-76492006-036.
Fowles, J., Burley, S., 1994. Textural and permeability characteristics of faulted, high porosity sandstones. Mar. Petrol. Geol. 11, 608–623. https://doi.org/10.1016/0264-8172(94)90071-X.
Gibson, R.G., 1998. Physical Character and fluid-flow Properties of sandstone-derived Fault Zones, vol. 127. Geological Society, London, Special Publications, pp. 83–97. https://doi.org/10.1144/GSL.SP.1998.127.01.07.
Harbaugh, A.W., 2005. MODFLOW-2005, the U.S. Geological Survey Modular ground-water Model – the Ground-Water Flow Process. U.S. Geological Survey Techniques and Methods, pp. 6–A16.
Harbaugh, A.W., Langevin, C.D., Hughes, J.D., Niswonger, R.N., Konikow, L.F., 2017. MODFLOW-2005 Version 1.12.00, the U.S. Geological Survey Modular Groundwater Model. U.S. Geological Survey Software Release. https://doi.org/10.5066/F7RF5S7G, 03 February 2017.
Harper, T.R., Moftah, I., 1985. Skin effect and completion options in the Ras Budran Reservoir. In: Presented at the Middle East Oil Technical Conference and Exhibition. OnePetro. https://doi.org/10.2118/13708-MS.
Hsieh, P.A., 2001. TopoDrive and ParticleFlow–Two computer models for simulation and visualization of ground-water flow and transport of fluid particles. In: Two Dimensions: U.S. Geological Survey Open-File Report 01-286, p. 30. https://doi.org/10.3133/ofr01286.
Jourde, H., Flodin, E.A., Aydin, A., Durlofsky, L.J., Wen, X.-H., 2002. Computing permeability of fault zones in Eolian sandstone from outcrop measurements. AAPG (Am. Assoc. Pet. Geol.) Bull. 86, 1187–1200. https://doi.org/10.1306/61EEDC4C-173E-11D7-8645000102C1865D.
Khadri, S.F.R., Moharir, K., 2016. Characterization of aquifer parameter in basaltic hard rock region through pumping test methods: a case study of man river basin in Akola and Buldhana districts Maharashtra India. Model. Earth Syst. Environ. 2, 33. https://doi.org/10.1007/s40808-015-0047-9.
Manzocchi, T., Ringrose, P.S., Underhill, J.R., 1998. Flow Through Fault Systems in high-porosity Sandstones, vol. 127. Geological Society, London, Special Publications, pp. 65–82. https://doi.org/10.1144/GSL.SP.1998.127.01.06.
Marroni, M., Treves, B., 1998. Hidden terranes in the northern Apennines, Italy: a record of late cretaceous-oligocene transpressional tectonics. J. Geol. 106, 149–162. https://doi.org/10.1086/516013.
Matthäi, S.K., Aydin, A., Pollard, D.D., Roberts, S.G., 1998. Simulation of transient well-test signatures for geologically realistic faults in sandstone reservoirs. SPE J. 3, 62–76. https://doi.org/10.2118/38442-PA.
McBride, E.F., Milliken, K.L., Cavazza, W., Cibin, U., Fontana, D., Picard, M.D., Zuffa, G. G., 1995. Heterogeneous distribution of calcite cement at the outcrop scale in tertiary sandstones, northern apennines, Italy1. AAPG (Am. Assoc. Pet. Geol.) Bull. 79, 1044–1062. https://doi.org/10.1306/8D2B21C3-171E-11D7-8645000102C1865D.
Medici, G., Ling, F., Shang, J., 2023. Review of discrete fracture network characterization for geothermal energy extraction. Front. Earth Sci. 11, 1328397. https://doi.org/10.3389/feart.2023.1328397.
Mollema, P.N., Antonellini, M.A., 1996. Compaction bands: a structural analog for anti-mode I cracks in aeolian sandstone. Tectonophysics 267 (1–4), 209–228. https://doi.org/10.1016/S0040-1951(96)00098-4.
Mozley, P.S., Davis, J.M., 2005. Internal structure and mode of growth of elongate calcite concretions: evidence for small-scale, microbially induced, chemical heterogeneity in groundwater. Geol. Soc. Am. Bull. 117 (11–12), 1400–1412.
Nogueira, F.C.C., Nicchio, M.A., Balsamo, F., Souza, J.A.B., Silva, I.V.L., Bezerra, F.H.R., Vasconcelos, D.L., Carvalho, B.R.B.M., 2021. The influence of the cataclastic matrix on the petrophysical properties of deformation bands in arkosic sandstones. Mar. Petrol. Geol. 124, 104825. https://doi.org/10.1016/j.marpetgeo.2020.104825.
Ori, G.G., Friend, P.F., 1984. Sedimentary basins formed and carried piggyback on active thrust sheets. Geology 12, 475–478. https://doi.org/10.1130/0091-7613(1984)12<475:SBFACP>2.0.CO;2.
Pérez-Illanes, R., Fernàndez-Garcia, D., 2023. Multiprocessing for the particle tracking model MODPATH. Groundwater 61, 733–742. https://doi.org/10.1111/gwat.13279.
Piazza, A., Artoni, A., Ogata, K., 2016. The Epiligurian wedge-top succession in the Enza Valley (Northern Apennines): evidence of a syn-depositional transpressive system. Swiss J. Geosci. 109, 17–36. https://doi.org/10.1007/s00015-016-0211-x.
Pollock, D.W., 2016. User guide for MODPATH version 7—A particle-tracking model for MODFLOW. U.S. Geological Survey Open-File Report 2016–1086 35. https://doi.org/10.3133/ofr20161086.
Pollock, D.W., 2017. MODPATH v7.2.01: a particle-tracking model for MODFLOW: U.S. Geological Survey Software Release. https://doi.org/10.5066/F70P0X5X, 15 December 2017.
Pourmalek, A., Newell, A.J., Shariatipour, S.M., Butcher, A.S., Milodowski, A.E., Bagheri, M., Wood, A.M., 2021. Deformation bands in high-porosity sandstones: do they help or hinder CO2 migration and storage in geological formations? Int. J. Greenh. Gas Control 107, 103292. https://doi.org/10.1016/j.ijggc.2021.103292.
QGIS Development Team, 2021. QGIS geographic information system. Open Source Geospatial Foundation. URL. http://qgis.org.
Rawling, G.C., Goodwin, L.B., 2003. Cataclasis and particulate flow in faulted, poorly lithified sediments. J. Struct. Geol. 25, 317–331. https://doi.org/10.1016/S0191-8141(02)00041-X.
Rawling, G.C., Goodwin, L.B., Wilson, J.L., 2001. Internal architecture, permeability structure, and hydrologic significance of contrasting fault-zone types. Geology 29, 43–46. https://doi.org/10.1130/0091-7613(2001)029<0043:IAPSAH>2.0.CO;2.
Remitti, F., Bettelli, G., Panini, F., Carlini, M., Vannucchi, P., 2012. Deformation, fluid flow, and mass transfer in the forearc of convergent margins: a two-day field trip in an ancient and exhumed erosive convergent margin in the northern Apennines, in: deformation, fluid flow, and mass transfer in the forearc of convergent margins: field guides to the northern Apennines. In: Emilia and in the Apuan Alps (Italy). Geological Society of America, pp. 1–33. https://doi.org/10.1130/2012.0028(01.
Ricci Lucchi, F., 1986. The Oligocene to recent foreland basins of the Northern Apennines. In: Foreland Basins. John Wiley & Sons, Ltd, pp. 103–139. https://doi.org/10.1002/9781444303810.ch6.
Romano, C., Garing, Minto, J.M., Benson, S.M., Shipton, Z.K., Lunn, R.J., 2021. Extreme capillary heterogeneities and in situ fluid compartmentalization due to clusters of deformation bands in sandstones. Int. J. Greenh. Gas Control 106, 103280. https://doi.org/10.1016/j.ijggc.2021.103280.
Rotevatn, A., Fossmark, H.S., Bastesen, E., Thorsheim, E., Torabi, A., 2017. Do deformation bands matter for flow? Insights from permeability measurements and flow simulations in porous carbonate rocks. Pet. Geosci. 23, 104–119. https://doi.org/10.1144/petgeo2016-038.
Rotevatn, A., Sandve, T.H., Keilegavlen, E., Kolyukhin, D., Fossen, H., 2013. Deformation bands and their impact on fluid flow in sandstone reservoirs: the role of natural thickness variations. Geofluids 13, 359–371. https://doi.org/10.1111/gfl.12030.
Salvini, F., 2002. Daisy 3: the structural data integrated system analyzer. Dipartimento di Scienze Geologiche Università di "Roma Tre,". Roma.
Shipton, Z.K., Evans, J.P., Thompson, L.B., 2005. The geometry and thickness of deformation-band fault core and its influence on sealing characteristics of deformation-band fault zones, 181–195. https://doi.org/10.1306/1033723M853135.
Souza, F.M.D., Gomes, I.F., Nogueira, F.C.C., Vasconcelos, D.L., Canabarro, B., Souza, J. A.B.D., Guimarães, L.J.D.N., Beserra, L.B.D.S., 2022. 2D modeling and simulation of deformation bands' effect on fluid flow: implications for hydraulic properties in siliciclastic reservoirs. J. Struct. Geol. 158, 104581. https://doi.org/10.1016/j.jsg.2022.104581.
Sternlof, K.R., Chapin, J.R., Pollard, D.D., Durlofsky, L.J., 2004. Permeability effects of deformation band arrays in sandstone. AAPG (Am. Assoc. Pet. Geol.) Bull. 88, 1315–1329.
Sternlof, K.R., Karimi-Fard, M., Pollard, D.D., Durlofsky, L.J., 2006. Flow and transport effects of compaction bands in sandstone at scales relevant to aquifer and reservoir management. Water Resour. Res. 42. https://doi.org/10.1029/2005WR004664.
Stendardi, F., Viola, G., Vignaroli, G., 2023. Multiscale structural analysis of an Epiligurian wedge-top basin: insights into the syn-to post-orogenic evolution of the northern Apennines accretionary wedge (Italy). Int. J. Earth Sci. 112 (3), 805–827. https://doi.org/10.1016/j.advwatres.2018.02.016.
Sutton, C.R., Zahasky, C., 2025. A laboratory-validated, graph-based flow and transport model for naturally fractured media. Geophys. Res. Lett. 52 (1), e2024GL112277. https://doi.org/10.1029/2024GL112277.
Taylor, W.L., Pollard, D.D., 2000. Estimation of in situ permeability of deformation bands in porous sandstone, Valley of fire, Nevada. Water Resour. Res. 36, 2595–2606. https://doi.org/10.1029/2000WR900120.
Taylor, W.L., Pollard, D.D., Aydin, A., 1999. Fluid flow in discrete joint sets: field observations and numerical simulations. J. Geophys. Res. Solid Earth 104, 28983–29006. https://doi.org/10.1029/1999JB900179.
Torabi, A., Fossen, H., 2009. Spatial variation of microstructure and petrophysical properties along deformation bands in reservoir sandstones. AAPG (Am. Assoc. Pet. Geol.) Bull. 93, 919–938. https://doi.org/10.1306/03270908161.
Vai, G.B., Martini, I.P., 2001. Geomorphologic settings. In: Vai, G.B., Martini, I.P. (Eds.), Anatomy of an Orogen: the Apennines and Adjacent Mediterranean Basins. Springer, Netherlands, Dordrecht, pp. 1–4. https://doi.org/10.1007/978-94-015-9829-3_1.
Valloni, R., Zuffa, G.G., 1984. Provenance changes for arenaceous formations of the northern Apennines, Italy. GSA Bulletin 95, 1035–1039. https://doi.org/10.1130/0016-7606(1984)95<1035:PCFAFO>2.0.CO;2.
Winston, R.B., 2019. ModelMuse version 4—A graphical user interface for MODFLOW 6: U.S. Geological Survey Scientific Investigations Report 10. https://doi.org/10.3133/sir20195036, 2019–5036.
Winston, R.B., 2020. ModelMuse version 4.2: U.S. Geological Survey software release, 25 February 2020. https://doi.org/10.5066/P9XMX92F.
Zambrano, M., Tondi, E., Mancini, L., Lanzafame, G., Trias, F.X., Arzilli, F., et al., 2018. Fluid flow simulation and permeability computation in deformed porous carbonate grainstones. Adv. Water Resour. 115, 95–111. https://doi.org/10.1016/j.advwatres.2018.02.016.
Zambrano, M., Volatili, T., Mancini, L., Pitts, A., Giorgioni, M., Tondi, E., 2021. Pore-scale dual-porosity and dual-permeability modeling in an exposed multi-facies porous carbonate reservoir. Mar. Petrol. Geol. 128, 105004. https://doi.org/10.1016/j.marpetgeo.2021.105004.
Zheng, C., 2002. TopoDrive and particle flow: simple tools for learning ground water modeling. (Software Spotlight). Ground Water 40, 222–224.
Zuluaga, L.F., Rotevatn, A., Keilegavlen, E., Fossen, H., 2016. The effect of deformation bands on simulated fluid flow within fault-propagation fold trap types: lessons from the San Rafael monocline, Utah. AAPG (Am. Assoc. Pet. Geol.) Bull. 100, 1523–1540. https://doi.org/10.1306/04151614153.